ACS APPLIED MATERIALS & INTERFACES

Research Article

www.acsami.org

Strain Accommodation by Facile WO_6 Octahedral Distortion and Tilting during WO_3 Heteroepitaxy on $SrTiO_3$(001)

Yingge Du,*[,†] Meng Gu,[†] Tamas Varga,[†] Chongmin Wang,[†] Mark E. Bowden,[†] and Scott A. Chambers[‡]

[†]Environmental Molecular Sciences Laboratory and [‡]Fundamental and Computational Sciences Directorate, Pacific Northwest National Laboratory, Richland, Washington 99352, United States

ABSTRACT: In this work, we demonstrate that WO_6 octahedra in tungsten trioxide (WO_3) undergo an unusually large degree of distortion and tilting to accommodate interfacial strain. This motion strongly impacts nucleation, structure, and defect formation during the epitaxial growth of WO_3 on $SrTiO_3$(001). A metastable tetragonal phase can be stabilized by heteroepitaxy and a thickness-dependent phase transition (tetragonal to monoclinic) is observed. In contrast to misfit dislocation formation, facile WO_6 octahedral deformation gives rise to three types of planar defects. The thicknesses of affected regions can range from several to tens of nanometers with graded lattice parameters, allowing the strain from interfacial lattice mismatch to be relieved gradually. These atomically resolved, unique interfacial defects may significantly alter the electronic, electrochromic, and mechanical properties of WO_3 epitaxial films.

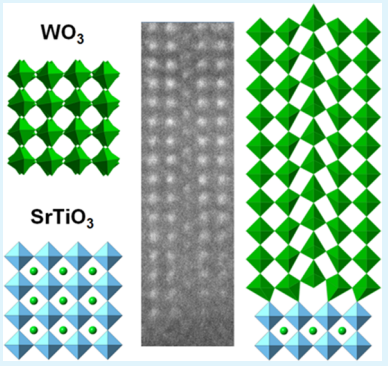

KEYWORDS: *WO_3, epitaxy, tungsten oxide, octahedral distortion, $SrTiO_3$*

1. INTRODUCTION

The ability to modify and control the octahedral connectivity within perovskite-structured oxides has been intensively explored to engineer materials with desired properties and integrate multilayered structures into multifunctional devices.[1−3] The cubic perovskite crystal structure has the formula ABO_3 where the A-site atom sits at the cube center, surrounded by eight corner-sharing BO_6 octahedra, as shown in Figure 1a for $SrTiO_3$ (STO). In many cases, the stringent requirements for an ideal cubic structure cannot be met. Slight distortion, tilting, and/or rotation of the BO_6 octahedra can result in several distorted versions with lower symmetry, such as the orthorhombic and tetragonal phases. The properties of perovskite oxides are heavily dependent on the chemistry of the B-site transition metal as the A-site cations are normally of a fixed valence. Distortions in the BO_6 octahedra directly influence the B-site cation−oxygen bond length, angle, and connectivity, which in turn lead to a wide range of interesting properties, including ferroelectricity, ferromagnetism, and superconductivity.[1,4−7] The degree of distortion in most known perovskite structures is small, being limited by the large ionic radius of the A-site cation. Interestingly, the crystal structure of tungsten trioxide (WO_3) can be considered as pseudoperovskite where the A-site is empty, as shown in Figure 1b. From 100 to 1000 K, WO_3 undergoes at least five phase changes, including monoclinic, orthorhombic, and tetragonal, due to the tilting and distortion of the corner-sharing WO_6 octahedra.[8] WO_3 is thus an ideal model system for investigating BO_6 octahedral deformations. The structure of WO_3 epitaxial thin films can in principle be tailored by strain and substrate symmetry to allow stabilization of phases that are unstable or nonexistent in the bulk. Such studies can be of significant technological relevance as applications such as gas sensors, catalysts, and electrochromic materials are critically dependent on crystal structure.[8−12]

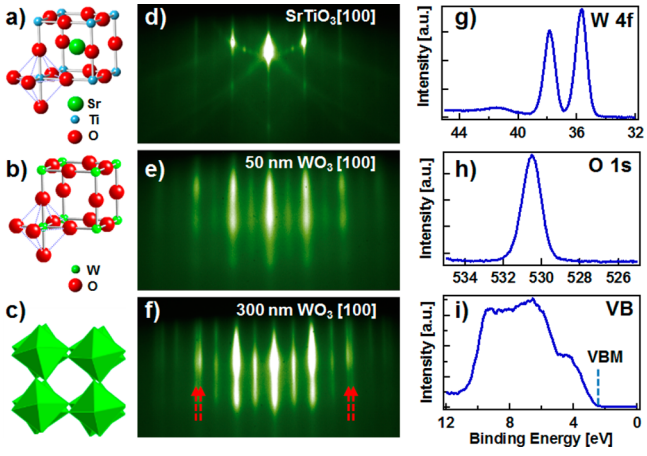

Figure 1. Structural models of $SrTiO_3$ (a) and WO_3 (b), each with a BO_6 octahedron in the bottom corner. Monoclinic tungsten trioxide (c) exhibits a corner-sharing network of distorted WO_6 octahedra. Reflection high-energy electron diffraction (RHEED) patterns taken along the [100] azimuthal direction for the following: $SrTiO_3$(001) (d), 50 nm WO_3 (e), and 300 nm WO_3 (f). Core-level W 4f (g), O 1s (h), and valence band (i) XPS spectra for the 50 nm WO_3 film.

Received: June 5, 2014
Accepted: July 24, 2014
Published: July 24, 2014

In the bulk, WO_3 is monoclinic at room temperature, as shown in Figure 1c, with lattice parameters a = 7.30 Å, b = 7.54 Å, c = 7.69 Å, and β = 90.9°. This lattice represents a 2 × 2 × 2 superstructure consisting of simplified cubic unit cells (u.c.) of dimension ~3.70−3.75 Å.[8,13] Heteroepitaxy has been shown to be effective in tuning the film/substrate interface through interfacial strain and thus dictating the crystal structure of the resulting WO_3 films. For example, by varying growth temperature and orientation of sapphire substrates, epitaxial WO_3 films have been shown to nucleate as tetragonal, monoclinic, and hexagonal phases.[14,15] STO is a cubic perovskite widely used as an oxide single-crystal substrate for thin-film studies. $WO_3/SrTiO_3$ has been proposed as a photocatalyst material system with potential for energy storage,[16] and WO_3 heteroepitaxy on STO(001) by magnetron sputtering has been demonstrated.[17] X-ray diffraction (XRD) and transmission electron microscopy (TEM) yielded crucial information for structural determination of stoichiometric WO_3 and the associated Magnéli phases, which are intermediate, reduced structures.[18−20] However, the interfaces between WO_3 and these various substrates have not been thoroughly characterized or understood.[21] It is important to understand whether WO_3 epitaxial films are coherently strained to their substrates or whether the strain can be released through defect formation. Also, it is of fundamental importance to explore the extent to which the interface can stabilize WO_3 films in certain phases that are otherwise unstable. In this work, we report the epitaxial growth and characterization of WO_3 thin films on STO(001). We find that film crystallography, film/substrate interface structure, and defect formation are directly connected to WO_6 octahedral deformation.

2. RESULTS AND DISCUSSION

The reflection high-energy electron diffraction (RHEED) patterns were recorded for clean substrates and then only intermittently during and after the growth of each film. The RHEED patterns for a clean STO(001) substrate and for 50 and 300 nm WO_3 films along the [100] azimuthal direction are shown in Figure 1d−f. The 50 nm WO_3 film displays sharp diffraction streaks aligned with those from STO, indicating the epitaxial relationship $(001)_{WO_3}||(001)_{STO}$ and $[100]_{WO_3}||[100]_{STO}$, as well as a smooth surface. Similar streaks are observed for the 300 nm film. However, a distinct splitting is seen corresponding to multiple in-plane lattice parameters, as marked by the red arrows in Figure 1f.

Core-level W 4f, O 1s, and valence band XPS spectra of the two films are identical, and thus, only the 50 nm spectra are shown in Figure 1g−i. The W 4f spectrum is well fit by a spin−orbit split doublet at 45.6 and 47.7 eV. The O 1s spectrum can be fit by a single peak at 530.5 eV. Both are in agreement with reported values in the literature for stoichiometric WO_3.[22,23] No density of state near the Fermi level is observed in the valence bond (VB) spectrum, indicating that the W atoms are in the 6+ oxidation state with the characteristic $5d^0$ configuration. These results reveal that the film surfaces are fully oxidized and free of W^{5+} or W^{4+} within the detection limit of XPS.

The XRD patterns for the two films are shown in Figure 2. The out-of-plane θ−2θ scan for the 50 nm film (Figure 2a) contains a single set of (00l) film peaks along with the sharper substrate peaks. The out-of-plane lattice parameter (c) is 3.6772(1) Å. In-plane reflections (not shown) are consistent

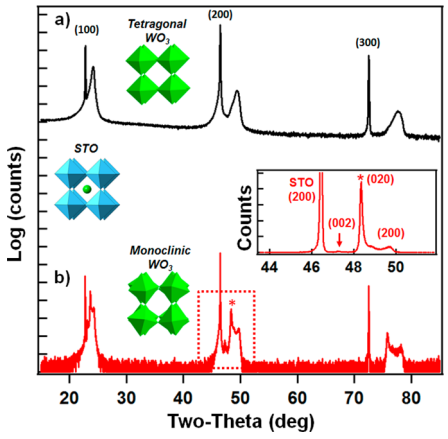

Figure 2. XRD θ−2θ scans for 50 nm (a) and 300 nm (b) WO_3 films on $SrTiO_3$(001). A magnified view with a linear intensity scale measured between 44 and 52° is shown as an inset for the 300 nm film. Patterns collected using Cu Kα radiation (1.54056 Å).

with a tetragonal structure with an in-plane lattice parameter (a) of 3.818(3) Å as determined using θ−2θ scans of the (113) and (301) peaks. Nucleation of the tetragonal phase is most likely driven by tensile strain due to in-plane lattice mismatch with the STO substrate. This tetragonal structure is similar to that seen in the growth of WO_3 on r-cut $Al_2O_3(01\bar{1}2)$,[15] but different from the WO_3/STO results reported earlier,[17] where the monoclinic phase was found to nucleate at a growth temperature of 500 °C. The ~3.68 Å out-of-plane parameter derived from Figure 2a is significantly smaller than previously reported values for the tetragonal phase (c > 3.90 Å),[15,17,24] or cubic phase (reported c values ranges from 3.71 to 3.84 Å).[21,25] The a value is smaller than that for STO, revealing that the film is not coherently strained. The XRD data shown in Figure 2b reveal three different out-of-plane lattice spacings for the 300 nm thick film. The difference in signal-to-noise between the two patterns in Figure 2 is a consequence of the different detectors used. For the tetragonal film we used the simple slit detector to give larger peak intensities. To resolve the out-of-plane peaks for the monoclinic film, we used an analyzer crystal detector which reduced the signal as well as the background compared to the slit detector. The spacings near 47−50° 2θ were 3.69, 3.76, and 3.84 Å, which are close to the lattice parameters of the bulk monoclinic phase (a/2 = 3.65 Å, b/2 = 3.77 Å, and c/2 = 3.85 Å). This suggests that the thicker film has transformed to monoclinic WO_3 with small differences in lattice parameters, most likely due to the influence from the substrate.[15] It should be noted that the out-of-plane peak corresponding to 3.76 Å (labeled by an asterisk (*)) is much stronger than the other two. This predominance can be seen more clearly when the y axis is plotted on a linear scale, as seen as the inset in Figure 2, and indicates that the film is predominantly aligned with b out-of-plane with respect to the substrate.

To better understand this thickness-dependent phase transition and to quantitatively compare the in-plane lattice parameters with XRD data, four representative RHEED patterns recorded at different thicknesses during the 300 nm film growth are analyzed in Figure 3a−d. Line profiles measured at a common position shown in Figure 3a are displayed in the panel below. Using the STO substrate as an internal standard to calibrate the in-plane lattice parameter scale (black dotted lines), the in-plane lattice parameters for the 10

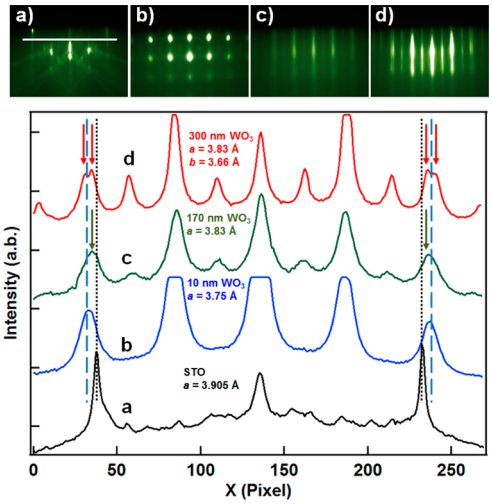

Figure 3. RHEED patterns taken along the [100] azimuthal direction for a STO substrate (a), along with WO_3 films of thicknesses 10 (b), 170 (c), and 300 nm (d). The line profiles are displayed in the bottom panel for each pattern as marked.

and 170 nm films are estimated to be 3.75 Å (blue dashed lines) and 3.83 Å (indicated by black arrows), respectively. The spotty pattern (Figure 3b) displayed for the 10 nm film indicates epitaxial island growth. Three-dimensional (3D) island growth usually involves a complex interplay between stress generation and relaxation,[26] and when the island dimensions are smaller than the attenuation length for the 15 keV incident RHEED beam, the pattern is dominated by transmission through those islands. The initial WO_3 islands are most likely relaxed as the in-plane lattice parameter (a = 3.75 Å) is much (~4%) smaller than that of the STO. If the interface strain relaxation is estimated by a simple stiff ball-and-stick model, a dislocation is expected every ~25 u.c. along the [100] or [010] direction. In contrast, the 170 nm film, along with the 50 nm film (Figure 1e), display streaky patterns, meaning that either the terraces of the islands are large enough to give rise to the coherent surface diffraction, or the islands have merged into continuous films. The latter is found to be the case by cross-sectional TEM imaging (not shown). For the continuous 170 nm film, the a lattice parameter is 3.83 Å, slightly larger than that of the 10 nm islands, likely due to further stress generation during coalescence of the discrete islands.[26,27] The diffraction streaks for the 300 nm film are split into two peaks, one aligned with the streaks for the 170 nm film, indicating an in-plane lattice parameter of 3.83 Å, and a second of equal intensity corresponding to 3.66 Å. These values are rather close to those for the predominantly in-plane lattice parameters revealed by XRD for the monoclinic phase (Figure 2b), 3.69 and 3.84 Å. The phase transition from tetragonal to monoclinic indicates that the influence of the substrate, which drives nucleation of the tetragonal phase for smaller film thicknesses, is lost at higher film thicknesses and the bulk phase prevails. Interestingly, a thickness-dependent phase transition was also observed for WO_3/Al_2O_3, but in the reverse order,[15] where a monoclinic phase appeared first followed by a dominant (002)-oriented phase. In our case, the cubic symmetry and tensile strain imposed by the STO substrate leads to WO_6 octahedral distortion and tilting such that a metastable tetragonal phase is stabilized. However, the interface is incoherent as shown by XRD and RHEED data. Strain energy release can occur via formation of cation or oxygen vacancies, misfit dislocations, or planar defects during the film growth process. As a result, mismatch-driven strain is gradually released until the film achieves its bulk structure. On the other hand, if the substrate effect can be removed, bulk-stable monoclinic structure should form even at a low thickness, as observed in atomically thin WO_3 sheets synthesized from hydrated tungsten trioxide.[28]

The STEM measurements were performed on the 50 nm film. In order to illustrate the defect structure that occurs, we first discuss a nonrepresentative coherently strained area. Figure 4 shows a STEM image of a well ordered, defect-free region

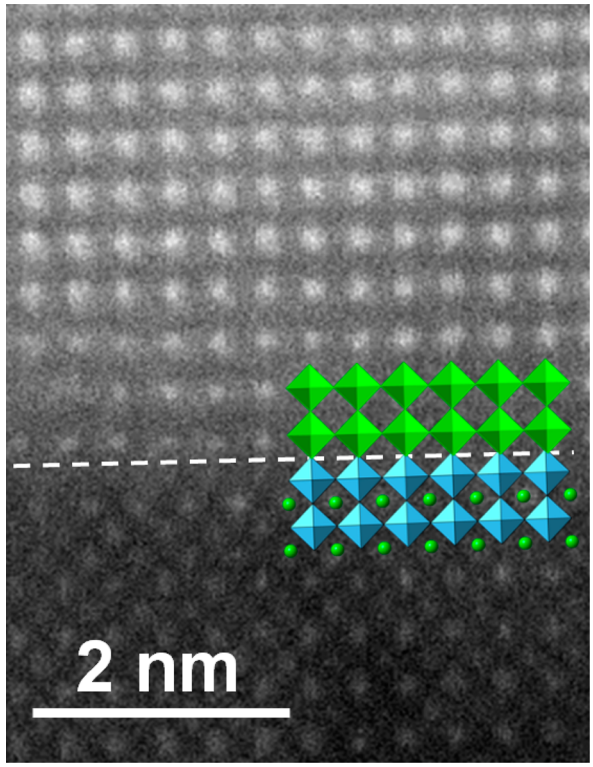

Figure 4. STEM image and corresponding structural model in a coherently strained region of the interface between epitaxial WO_3 and $SrTiO_3(001)$ with the interface marked by a dashed line. The color scheme for the polyhedral model is the same as that used in Figure 2.

containing the epitaxial interface (marked by the dashed line) and WO_3 crystal structure (top). Tungsten atoms appear much brighter in STEM due to the higher atomic number. Because the surface preparation leads to a TiO_2-terminated STO surface, each W atom connects to a Ti atom through an O as shown in the structural model. No dislocations or visible lattice distortions are observed in this region, and the WO_3 film appears to be coherently strained to the STO substrate. There is some dark-field intensity from interstitial sites in the WO_3 film within the first two to three layers from the interface, presumably because of Sr out-diffusion to form an interface phase of Sr_xWO_3, which would be similar in structure to strontium tungstate ($SrWO_3$ or $SrWO_4$).[29,30]

Compared to the coherently strained area shown in Figure 4, more typical interfacial regions contain significant concentrations of defects that can be categorized into three types, as shown in Figure 5. In one, there is a significant compression of a (100)-oriented plane of WO_3, as marked by the red arrow in Figure 5a. This displacement effectively reduces the density of

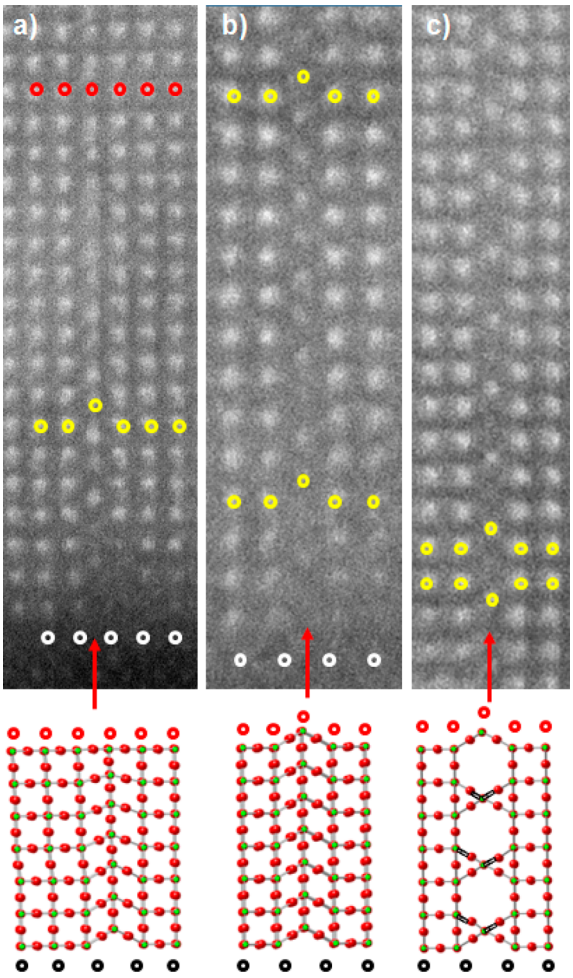

Figure 5. (a–c) Three types of planar defects revealed by STEM. The color scheme for the ball models is the same as that used in Figure 1.

W atoms at the interface, leaving five rows visible at the interface (marked by white circles), compared to six rows in the same field of view further away from the interface (marked by red circles). The W atoms in the compressed plane appear to shift half a u.c. along the [001] direction initially (refer to the yellow circle in Figure 5a), and the net amount of shift decreases as the layers build up. Some of the displaced W rows exhibit lower contrast, indicating that they may contain fewer atoms. After ~15 u.c., the compression subsides and W atoms in this plane are aligned with those in adjacent rows. The net effect of this displacement is similar to that resulting from a misfit dislocation at the interface, allowing the smaller lattice parameter of WO_3 to be accommodated at the interface, consistent with the smaller in-plane value measured by XRD and RHEED relative to that for STO. By forcing this kind of compression as opposed to generating a misfit dislocation, the tensile strain in the film is released gradually rather than abruptly. Additionally, the lattice distortion propagates much deeper into the film than it would in the case of misfit dislocation generation. For perovskite films on perovskite substrates, such as $SrZrO_3$ and BaTiO3 on STO(001),[31,32] formation of dislocations has been determined to be the main mechanism to release the lattice mismatch induced strain. It should be noted in those studies, the high-resolution TEM revealed that only the nearest atoms (within 1–2 monolayers (MLs)) adjacent to the dislocations were affected. The unusual accommodation of mismatch in WO_3 occurs most likely because of the ease with which WO_6 octahedra can distort due to the absence of A-site cations, as manifested in highly deformed Magnéli phases.[18−20]

The second type of planar defect, shown in Figure 5b, is similar to that shown in Figure 5a. However, the displacement stays constant at 0.5 u.c. and persists for more than 20 u.c. In this case, the epitaxial strain is released through film buckling as shown in the structural model.

The third type of defect, shown in Figure 5c, also penetrates deeper into the film with W rows shifted by 0.5 u.c. in the [100] direction. The STEM image was taken ~10 MLs away from the film/substrate interface. The difference between type 2 and type 3 is that, in type 3, W rows are missing in every other layer, as marked by the yellow circles. The W rows near the defect plane form a series of connected hexagons, somewhat similar to the (001)-oriented WO_3 hexagonal phase. If the planar defects shown in Figure 5b,c are present throughout the film, line defects running along ⟨100⟩ directions can be expected on the (001) surface, which may appear similar to the line defects observed by earlier STM studies on single-crystal WO_3(001).[13] All three planar defect structures shown in Figure 5 lead to lattice relaxation through the formation of a structurally modified plane. From the limited statistics available by STEM, the average distance between two planar defects is ~20 u.c., comparable with the 25 u.c. estimated from the RHEED pattern (Figure 3b) discussed earlier. The formation of such defective structures requires a large degree of distortion of the WO_6 octahedra, which would not be feasible in most other perovskites because of the presence of "A"-site cations. The angle and length of various W–O–W bonds in the three models are significantly altered from a cubic or tetragonal symmetry.

3. CONCLUSION

In summary, we have investigated the unusual nucleation habits of epitaxial WO_3 films on STO(001) using multiple techniques. We show that lattice mismatch in the metastable tetragonal phase, which initially forms, is accommodated by extraordinary flexibility in WO_3 made possible by the ability of WO_6 octahedra to distort. This flexibility is a result of the absence of A-site cations, and it makes WO_3 an ideal material for gaining insight into the phenomena of octahedral distortions in perovskites. Indeed, the formation of the tetrahedral phase at the interface is made possible by the octahedral stretching (increase in bond length) and tilting from the bulk monoclinic structure, which dominates at higher film thicknesses. Three types of planar defects which accommodate in-plane lattice misfit have been observed. Formation of these defects involves WO_6 distortion as well as changes in octahedral connectivity, as manifested by changes in bond angles and symmetry. The changes in WO_6 octahedral distortion and connectivity may significantly alter the electronic, electrochromic, and mechanical properties of the WO_3 films. These experimental results should stimulate significant interest in theoretically modeling WO_3 to learn more about the effect of these structural variants on functional properties.

4. EXPERIMENTAL SECTION

Epitaxial WO_3 thin films were grown on (001)-oriented, Nb-doped $SrTiO_3$ (Nb-STO, a_{STO} = 3.905 Å) substrates by oxygen plasma assisted molecular beam epitaxy. High-purity WO_3 powders (Sigma-Aldrich, >99.99%) were evaporated from a high-temperature effusion

cell to provide a film growth rate of ~0.1 Å/s as calibrated by a quartz crystal microbalance. The substrates were etched and annealed to obtain TiO_2-terminated surfaces prior to each growth and annealed in O plasma (with the O_2 partial pressure in the chamber set at ~3 × 10^{-6} Torr) at 500 °C to remove surface contaminates. The substrate temperature during growth was 500 °C, and oxygen plasma was maintained at the same settings during each film growth to prevent O vacancy formation. RHEED patterns were taken only as needed to avoid electron-beam-induced changes to the film surface, which will be described elsewhere. WO_3 films were characterized *in situ* by high-resolution X-ray photoelectron spectroscopy (XPS) using a monochromatic Al Kα X-ray source and a VG Scienta R3000 electron energy analyzer. Epitaxial relationship, crystalline quality, and lattice parameters were investigated using high-resolution XRD with a Philips X'Pert Materials Research diffractometer (MRD) equipped with a fixed Cu anode operating at 45 kV and 40 mA. A hybrid monochromator, consisting of four-bounce double-crystal Ge (220) and a Cu X-ray mirror, was placed in the incident beam path to generate monochromatic Cu Kα X-rays (λ = 1.54056 Å) with a beam divergence of 12 arc seconds. The diffracted beam was detected using a 0.38 mm slit for the tetragonal sample (Figure 2a), and with a three-bounce analyzer crystal for the monoclinic sample (Figure 2b). For scanning transmission electron microscopy (S/TEM) imaging, an FEI-Titan 80-300 microscope equipped with a probe forming lens corrector was used. The image was taken with an accelerating voltage of 300 keV. The high annular dark-field (HAADF) image collection angle is 50−200 mrad. It is known that WO_3 films can reduce under ion and electron beam irradiation,[33−35] which typically occurs during the preparation of the thin section by focused ion beam milling and subsequent TEM imaging. To avoid ion and electron beam damage to the WO_3 film, we prepared the sample by mechanical thinning followed by Ar ion sputtering at low energy and performed STEM imaging with the minimum dwell time.

AUTHOR INFORMATION

Corresponding Author

*E-mail: yingge.du@pnnl.gov.

Notes

The authors declare no competing financial interest.

ACKNOWLEDGMENTS

The work was performed using the Environmental Molecular Sciences Laboratory, a national scientific user facility, sponsored by the Department of Energy's Office of Biological and Environmental Research, located at Pacific Northwest National Laboratory. Y.D. gratefully acknowledges support by EMSL's Intramural Research and Capability Development Program. A portion of the work was supported by the Office of Basic Energy Sciences, Division of Materials Science and Engineering under Award 10122. M.G. and C.W. are thankful for the support by the Joint Center for Energy Storage Research (JCESR), an Energy Innovation Hub funded by the U.S. Department of Energy, Office of Science, Basic Energy Sciences. The authors thank Ping Yang, Tim Droubay, and Kelvin H. L. Zhang for many insightful discussions.

REFERENCES

(1) Rondinelli, J. M.; May, S. J.; Freeland, J. W. Control of Octahedral Connectivity in Perovskite Oxide Heterostructures: An Emerging Route to Multifunctional Materials Discovery. *MRS Bull.* **2012**, *37*, 261−270.

(2) Aso, R.; Kan, D.; Shimakawa, Y.; Kurata, H. Atomic Level Observation of Octahedral Distortions at the Perovskite Oxide Heterointerface. *Sci. Rep.* **2013**, *3*, No. 2214.

(3) He, J.; Borisevich, A.; Kalinin, S. V.; Pennycook, S. J.; Pantelides, S. T. Control of Octahedral Tilts and Magnetic Properties of Perovskite Oxide Heterostructures by Substrate Symmetry. *Phys. Rev. Lett.* **2010**, *105*, No. 227203.

(4) Cohen, R. E. Origin of Ferroelectricity in Perovskite Oxides. *Nature* **1992**, *358*, 136−138.

(5) Nan, C. W.; Bichurin, M. I.; Dong, S. X.; Viehland, D.; Srinivasan, G. Multiferroic Magnetoelectric Composites: Historical Perspective, Status, and Future Directions. *J. Appl. Phys.* **2008**, *103*, No. 031101.

(6) Mulder, A. T.; Benedek, N. A.; Rondinelli, J. M.; Fennie, C. J. Turning ABO_3 Antiferroelectrics into Ferroelectrics: Design Rules for Practical Rotation-Driven Ferroelectricity in Double Perovskites and $A_3B_2O_7$ Ruddlesden-Popper Compounds. *Adv. Funct. Mater.* **2013**, *23*, 4810−4820.

(7) Rondinelli, J. M.; Fennie, C. J. Octahedral Rotation-Induced Ferroelectricity in Cation Ordered Perovskites. *Adv. Mater.* **2012**, *24*, 1961−1968.

(8) Zheng, H. D.; Ou, J. Z.; Strano, M. S.; Kaner, R. B.; Mitchell, A.; Kalantar-Zadeh, K. Nanostructured Tungsten Oxide—Properties, Synthesis, and Applications. *Adv. Funct. Mater.* **2011**, *21*, 2175−2196.

(9) Granqvist, C. G. Electrochromic Materials—Microstructure, Electronic Bands, and Optical-Properties. *Appl. Phys. A: Mater. Sci. Process.* **1993**, *57*, 3−12.

(10) Granqvist, C. G. Progress in Electrochromics: Tungsten Oxide Revisited. *Electrochim. Acta* **1999**, *44*, 3005−3015.

(11) Marsen, B.; Miller, E. L.; Paluselli, D.; Rocheleau, R. E. Progress in Sputtered Tungsten Trioxide for Photoelectrode Applications. *Int. J. Hydrogen Energy* **2007**, *32*, 3110−3115.

(12) Bondarchuk, O.; Huang, X.; Kim, J.; Kay, B. D.; Wang, L. S.; White, J. M.; Dohnalek, Z. Formation of Monodisperse $(WO_3)_3$ Clusters on TiO_2(110). *Angew. Chem., Int. Ed.* **2006**, *45*, 4786−4789.

(13) Jones, F. H.; Rawlings, K.; Foord, J. S.; Cox, P. A.; Egdell, R. G.; Pethica, J. B.; Wanklyn, B. M. W. Superstructures and Defect Structures Revealed by Atomic-Scale STM Imaging of WO_3(001). *Phys. Rev. B* **1995**, *52*, 14392−14395.

(14) LeGore, L. J.; Greenwood, O. D.; Paulus, J. W.; Frankel, D. J.; Lad, R. J. Controlled Growth of WO_3 Films. *J. Vac. Sci. Technol., A* **1997**, *15*, 1223−1227.

(15) Moulzolf, S. C.; Legore, L. J.; Lad, R. J. Heteroepitaxial Growth of Tungsten Oxide Films on Sapphire for Chemical Gas Sensors. *Thin Solid Films* **2001**, *400*, 56−63.

(16) Ohko, Y.; Saitoh, S.; Tatsuma, T.; Fujishima, A. $SrTiO_3$-WO_3 Photocatalysis Systems with an Energy Storage Ability. *Electrochem.* **2002**, *70*, 460−462.

(17) Garg, A.; Leake, J. A.; Barber, Z. H. Epitaxial Growth of WO_3 Films on $SrTiO_3$ and Sapphire. *J. Phys. D: Appl. Phys.* **2000**, *33*, 1048−1053.

(18) Booth, J.; Ekstrom, T.; Iguchi, E.; Tilley, R. J. D. Notes on Phases Occurring in the Binary Tungsten-Oxygen System. *J. Solid State Chem.* **1982**, *41*, 293−307.

(19) Bursill, L. A. Structure of Small Defects in Nonstoichiometric WO_{3-x}. *J. Solid State Chem.* **1983**, *48*, 256−271.

(20) Magneli, A. Structures of the ReO_3-Type with Recurrent Dislocations of Atoms—Homologous Series of Molybdenum and Tungsten Oxides. *Acta Crystallogr.* **1953**, *6*, 495−500.

(21) LeGore, L. J.; Lad, R. J.; Moulzolf, S. C.; Vetelino, J. F.; Frederick, B. G.; Kenik, E. A. Defects and Morphology of Tungsten Trioxide Thin Films. *Thin Solid Films* **2002**, *406*, 79−86.

(22) Deangelis, B. A.; Schiavello, M. X-ray Photoelectron-Spectroscopy Study of Nonstoichiometric Tungsten-Oxides. *J. Solid State Chem.* **1977**, *21*, 67−72.

(23) Bringans, R. D.; Hochst, H.; Shanks, H. R. Defect States in WO_3 Studied with Photoelectron-Spectroscopy. *Phys. Rev. B* **1981**, *24*, 3481−3489.

(24) Locherer, K. R.; Swainson, I. P.; Salje, E. K. H. Transition to a New Tetragonal Phase of WO_3: Crystal Structure and Distortion Parameters. *J. Phys.: Condens. Matter* **1999**, *11*, 4143−4156.

(25) Palatnik, L. S.; Obolyaninova, O. A.; Naboka, M. N. New Modifications of Tungsten Oxides. *Inorg. Mater. SSSR* **1973**, *9*, 718.

(26) Floro, J. A.; Hearne, S. J.; Hunter, J. A.; Kotula, P.; Chason, E.; Seel, S. C.; Thompson, C. V. The Dynamic Competition Between

Stress Generation and Relaxation Mechanisms During Coalescence of Volmer-Weber Thin Films. *J. Appl. Phys.* **2001**, *89*, 4886−4897.
(27) Petrov, I.; Barna, P. B.; Hultman, L.; Greene, J. E. Microstructural Evolution During Film Growth. *J. Vac. Sci. Technol., A* **2003**, *21*, S117−S128.
(28) Kalantar-zadeh, K.; Vijayaraghavan, A.; Ham, M.-H.; Zheng, H.; Breedon, M.; Strano, M. S. Synthesis of Atomically Thin WO_3 Sheets from Hydrated Tungsten Trioxide. *Chem. Mater.* **2010**, *22*, 5660−5666.
(29) Arab, M.; Lopes-Moriyama, L.; dos Santos, T. R.; de Souza, C. P.; Gavarri, J. R.; Leroux, C. Strontium and Cerium Tungstate Materials $SrWO_4$ and $Ce_2(WO_4)_3$: Methane Oxidation and Mixed Conduction. *Catal. Today* **2013**, *208*, 35−41.
(30) Verhaege, G.; Colin, R.; Exsteen, G.; Drowart, J. Mass Spectrometric Determination of Stability of Gaseous Molybdites Tungstites Molybdates and Tungstates of Magnesium Calcium Strontium and Tin. *Trans. Faraday Soc.* **1965**, *61*, 1372−1375.
(31) Langjahr, P. A.; Lange, F. F.; Wagner, T.; Ruhle, M. Lattice Mismatch Accommodation in Perovskite Films on Perovskite Substrates. *Acta Mater.* **1998**, *46*, 773−785.
(32) Sun, H. P.; Tian, W.; Pan, X. Q.; Haeni, J. H.; Schlom, D. G. Evolution of Dislocation Arrays in Epitaxial $BaTiO_3$ Thin Films Grown on (100) $SrTiO_3$. *Appl. Phys. Lett.* **2004**, *84*, 3298−3300.
(33) Xie, F. Y.; Gong, L.; Liu, X.; Tao, Y. T.; Zhang, W. H.; Chen, S. H.; Meng, H.; Chen, J. XPS Studies on Surface Reduction of Tungsten Oxide Nanowire Film by Ar^+ Bombardment. *J. Electron Spectrosc. Relat. Phenom.* **2012**, *185*, 112−118.
(34) McCartney, M. R.; Crozier, P. A.; Weiss, J. K.; Smith, D. J. Electron-Beam-Induced Reactions at Transition-Metal Oxide Surfaces. *Vacuum* **1991**, *42*, 301−308.
(35) Tamou, Y.; Tanaka, S. Formation and Coalescence of Tungsten Nanoparticles under Electron Beam Irradiation. *Nanostruct. Mater.* **1999**, *12*, 123−126.